

Toward Higher Voltage Solid-State Batteries by Metastability and Kinetic Stability Design

Luhan Ye, William Fitzhugh, Eva Gil-González, Yichao Wang, Yibo Su, Haoqing Su, Tianyu Qiao, Lu Ma, Hua Zhou, Enyuan Hu, and Xin Li*

The energy density of battery systems is limited largely by the electrochemical window of the electrolyte. Herein, the combined thermodynamic and kinetic effects of mechanically induced metastability are shown to greatly widen the operational voltage window of solid-state batteries based on ceramic-sulfide electrolytes. Solid electrolyte voltage stability up to 10 V is achieved with minimal degradation, far beyond the capability of organic liquid electrolytes. Furthermore, combined experiment, *ab initio* computation, and theoretical modeling identify the nature of mechanically constrained $\text{Li}_{10}\text{GeP}_2\text{S}_{12}$ decomposition both within the bulk and at interfaces with cathode materials at very high voltages. Previously unclear kinetic processes are identified that, when properly implemented, can potentially allow solid-state full cells with remarkably high operational voltages.

1. Introduction

The electrochemical window of the conventional (liquid) non-aqueous electrolytes (<5.0 V) limits the development of high-voltage battery systems.^[1,2] Traditional organic liquid electrolytes often suffer from severe electrochemical instability at voltages higher than 4.5 V.^[3,4] As a result, the energy storage horizon is limited to cathode materials with plateaus at around 4 V. The ever-increasing demand for batteries with higher energy densities, thus, prefers new electrolyte systems with higher voltage stability windows.

L. Ye, Dr. W. Fitzhugh, Dr. E. Gil-González, Y. Wang, Y. Su, H. Su, T. Qiao, Prof. X. Li
 John A. Paulson School of Engineering and Applied Sciences
 Harvard University
 Cambridge, MA 02138, USA
 E-mail: lixin@seas.harvard.edu

Dr. L. Ma
 National Synchrotron Light Source II
 Brookhaven National Laboratory
 Upton, NY 11973, USA

Dr. H. Zhou
 X-Ray Science Division
 Advanced Photon Source
 Argonne National Laboratory
 Lemont, IL 60439, USA

Dr. E. Hu
 Chemistry Division
 Brookhaven National Laboratory
 Upton, NY 11973, USA

 The ORCID identification number(s) for the author(s) of this article can be found under <https://doi.org/10.1002/aenm.202001569>.

DOI: 10.1002/aenm.202001569

Sulfur-based ceramic solid-state electrolytes have spurred great interests due to their high ionic conductivities.^[5] Among them, ceramic-sulfide solid electrolytes have been reported with conductivities of 12–25 mS cm⁻¹, which are similar to or even higher than traditional liquid electrolytes. Unfortunately, the intrinsic voltage window of ceramic-sulfide solid electrolytes is narrow (1.7–2.1 V).^[6] Despite this, previous works have reported that $\text{Li}_{10}\text{GeP}_2\text{S}_{12}$ (LGPS) or $\text{Li}_{9.54}\text{Si}_{1.74}\text{P}_{1.44}\text{S}_{11.7}\text{Cl}_{0.3}$ (LSPS-Cl) based batteries can be cycled up to 5 V with minimal degradation.^[7,8] These seemingly contradictory results remain one of the most pressing issues facing the solid-electrolyte

field. Attempts to explain this have focused on interface contact or cathode coating,^[9] electronic insulation,^[10,11] and lithiation/delithiation of electrolyte.^[12–14] However, it still lacks a quantitative explanation of the disparate results found in literatures in this field.

Many studies have correlated the electrochemical performance of solid-state battery, especially ionic conductivity, with stacking pressure and obtained new understandings of the system.^[15–20] Previously, we showed that mechanical constrictions, in the form of core-shell morphologies, could induce metastability in an expanded voltage range for both LGPS and LSPS.^[8,21–23] In this work, we utilize cell-level mechanical constrictions to better understand the nature of LGPS decay when charged to high voltages in full cell architectures. Through this approach, we identify, for the first time, that not only can mechanical constriction lead to thermodynamic metastability in an expanded window, but that it can also lead to kinetic stability up to the tool testing limit of 9.8 V.

Synchrotron X-ray diffraction (XRD) and X-ray absorption spectroscopy (XAS) are used to measure the structural changes of LGPS before and after high-voltage holds. The results show direct evidences of LGPS straining during these electrochemical processes. In addition to LGPS straining due to (de)lithiation, which shifts XRD peaks,^[12,14,24] strain broadening suggests the existence of small localized domains of highly strained regions. These small strained pockets inside LGPS particles are evidences of decomposed inclusions within the solid-electrolyte, for the first time providing direct experimental evidences to prior predictions of nucleated decay morphologies.^[21] The compositional nature of these small, highly strained domains are analyzed here by comparing density functional theory

(DFT) simulations and X-ray photoelectron spectroscopy (XPS) measurements. The results suggest that mechanically induced metastability stabilizes the LGPS up to ≈ 4 V, in agreement with previous works.^[8,21–23] In addition, from 4–10 V, the local stresses experienced by small local decompositions amid rigid mechanical constrictions lead to kinetic stability. Combined, mechanically induced metastability and kinetic stability allow the expansion of voltage window from 2.1 V^[6] to nearly 10 V.

To further understand the effects of such cell-level mechanical constrictions on full cell operation, including the effects on key electrolyte-cathode interfaces, we constructed constrained solid-state full cells. $\text{LiCo}_{0.5}\text{Mn}_{1.5}\text{O}_4$ (LCMO), $\text{LiNi}_{0.5}\text{Mn}_{1.5}\text{O}_4$ (LNMO), and LiCoO_2 (LCO) cathodes were paired with either $\text{Li}_4\text{Ti}_5\text{O}_{12}$ (LTO) or lithium metal anode to demonstrate and analyze the high-voltage stability of constrained LGPS and the multiple interfaces. Various strains in this solid-state battery system, including active materials, the solid electrolyte, and their interfaces, as well as battery cells, are discussed in depth from our unique perspective of mechanical constriction design. This gives, for the first time, a system-level picture of how mechanically induced metastability from each part influences the multiple chemical and electrochemical stabilities, and thus the battery performance. This work provides a critical insight on how mechanical constrictions can lead to mechanically induced metastability and, moreover, how mechanical constrictions can control decomposition kinetics to reach unparalleled voltages and more stable interfaces for advanced designs of ultra-high-voltage solid-state batteries in the future.

2. Results and Discussion

To demonstrate how mechanical constriction influences the electrochemical stability of LGPS, cyclic voltammetry (CV) tests of LGPS+C/LGPS/Li cells were performed (Figure 1a). Three LGPS+C/LGPS pellets were initially pressed with 78, 233, and 467 MPa, respectively, a Li_3PS_4 -coated lithium metal film is then attached to the pellet as the counter and reference electrode.^[8] It is known that only a low testing pressure (a few MPa) can be applied to such lithium metal anode, as higher pressures will cause the mechanical short, and the initial contact between Li_3PS_4 -coated Li and electrolyte is good enough without external pressure.^[16] The battery was then tested in normal Swagelok cells with a negligible external pressure of only a few MPa, giving a quasi-isobaric battery testing condition. In addition, one battery assembly of LGPS+C/LGPS/graphite-Li was initially pressed at 467 MPa and then tested in a homemade pressurized cell with the applied external pressure calibrated as 250 MPa when fastening the battery, enforcing a quasi-isovolumetric battery testing environment. Note that the graphite film covered lithium metal (Li/G) effectively prevents the penetration of lithium at these high pressures applied.^[22] On the contrary, high initial and testing pressures must be applied to the entire LGPS+C/LGPS/graphite/Li pellet in this case to maintain a close interface contact, especially on the lithium side. The density of the LGPS pellets after being initially pressed at 78, 233, and 467 MPa and then released are 62%, 69%, and 77% ($\pm 4\%$ from different pellets), respectively, of the theoretical density of single crystal LGPS, if the pressure was released right after

it is applied, due to reformed voids and porosity. If the pressure was held for a few hours, the density can be higher than 90% due to a more sufficient plastic creep. The morphology of LGPS pellets after pressing is shown in Figure S1a, Supporting Information. The density of pellet in the pressurized cell (with an external pressure constantly applied after the initial 467 MPa press) calculated from an in situ force–displacement measurement (Figure S1b,c, Supporting Information), however, is already close to 100% beyond 26 MPa external pressure.

As shown in Figure 1a, in CV, there exists a threshold voltage, beyond which each cell begins to severely decompose. These thresholds are 4.5, 5, and 5.8 V for those Swagelok cells initially pressed at 78, 233, and 467 MPa then released in the Swagelok battery test, respectively (Figure S2, Supporting Information). The pressurized cell, however, was charged up to 9.8 V and shows no severe decomposition. Those large peaks in the Swagelok batteries should be related to the weak constriction on the anode interface, since the lithium film is only attached to the pellet in the assembly and then tested at a low pressure. In contrast, the strong mechanical constriction condition is kept throughout the whole battery pellet with Li/G anode under a high pressure. In the low voltage and current region (Figure 1b), two decomposition peaks can be seen at ≈ 3 and ≈ 3.6 V for the Swagelok cells, where decreasing peak intensity is observed with increasing pressure applied in the initial press step. In contrast, the pressurized cell almost avoids these peaks. The peaks were also reported in other works,^[24] which represent the decomposition of small fraction of LGPS that resides on the surface of voids remaining in the pellet after the initial press. At these surfaces, mechanical constriction is weak, thus the LGPS can show certain limited decomposition, expanding into the void region, without causing any local pressure to form. As the applied initial press pressure is increased, these voids disappear either due to plastic deformation or elastic shrinkage. Finally, 0% porosity can be reached at a constantly applied external pressure in the pressurized cell (467 MPa@250 MPa). Note that 10 wt% carbon was added in the cathode region with LGPS, and these CV tests were performed at a slow rate of 0.1 mV s⁻¹.

The in situ resistance of batteries in these four cells was measured by impedance spectroscopy at different voltages during the CV tests (Figure 1c; Figure S3, Supporting Information). Consistent with previous understanding,^[5,17] higher pressure in the initial press step here is found to improve the contact among particles as reflected in the decreased porosity, and thus reduce the initial resistance in solid-state battery systems at 3 V in Figure 1c. However, when the CV test is scanned toward high voltages, the resistance increases much faster in the Swagelok cells, indicating that the LGPS in cathode undergoes certain decomposition under the condition of weak mechanical constriction. The decomposition lowers the conductivity of solid electrolyte and leads to a higher bulk-resistance, which is correlated with the decomposition current observed in Figure 1a, as the resistance ramps up at the voltage where high decomposition current occurs. There is almost no change of resistance, however, for the battery tested under the isovolumetric condition. Meanwhile, the increase of charge transfer resistance is also observed (Figure S3e,f, Supporting Information), as a result of worse interfaces after decompositions. This is the most notable when the battery is initially pressed

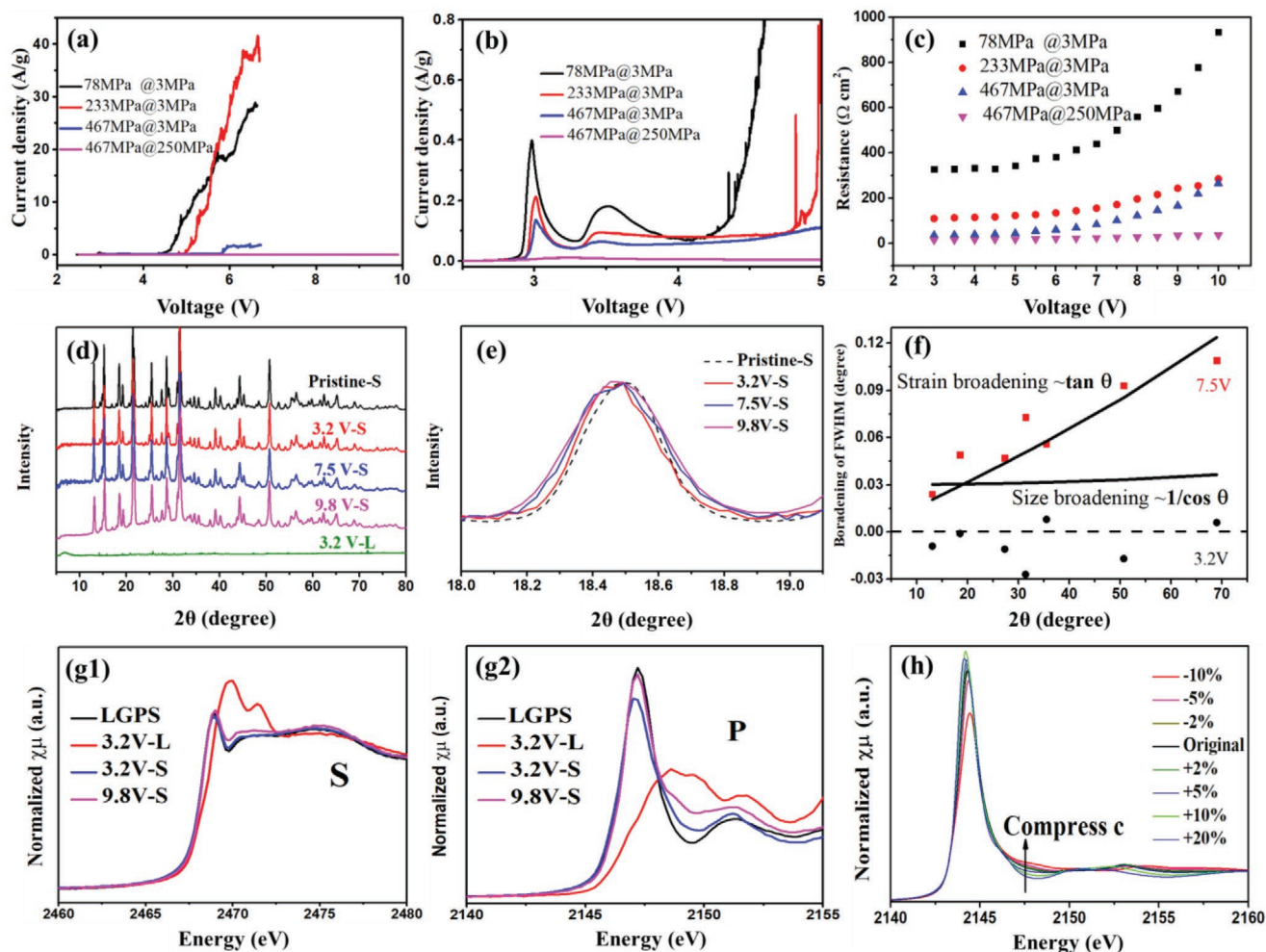


Figure 1. Stability of LGPS and the associated microstructure change. a) CV tests at 0.1 mV s^{-1} in Swagelok battery cells at negligible external pressure after they were initially pressed with 78 MPa (black), 233 MPa (red), 467 MPa (blue), then released in the Swagelok battery tests with the external pressure calibrated as 3 MPa, compared with the test under pressurized cell initially pressed at 467 MPa and tested at around 250 MPa (pink). 10% carbon is added in the cathode. The voltage range is set from open circuit to 9.8 V versus lithium metal. b) The CV scans in (a) plotted in a magnified voltage and current range. c) The bulk-resistance measured from in situ impedance tests at a 0.5 V step during CV scans for batteries shown in (a). The calculated charge transfer resistance is shown in Figure S3, Supporting Information. d) Synchrotron XRD of pressurized cells after no electrochemical process (black), CV scans to 3.2 V (red), 7.5 V (blue), and 9.8 V (pink). All CVs were followed by a voltage hold at the same high cut-off voltages for 10 h and then discharged back to 2.5 V. Green line: Synchrotron XRD of LGPS tested in a liquid electrolyte cell after CV scan to 3.2 V and held for 10 h. e) Synchrotron XRD peaks in (d) at $2\theta = 18.5^\circ$, illustrating the broadening of XRD peak after high-voltage CV scan and hold. f) Strain broadening and size broadening comparison analysis for LGPS after different voltage holds. Dots are the broadening of different Bragg peaks in a wide 2θ range from samples held at 7.5 V (red) and 3.2 V (black), with the corresponding XRD peaks shown in (d,e) and Figure S4, Supporting Information. The angle dependences of size and strain broadenings are represented by solid lines. g) XAS measurements of g1) S and g2) P peaks from LGPS after CV scans and holds at 3.2 V in liquid cell (3.2V-L), 3.2 V in solid cell (3.2V-S), and 9.8 V in solid cell (9.8V-S), compared with pristine LGPS. h) The simulation of P XAS peak changes by applying different strains in the c -direction of LGPS.

at 78 MPa and released (Figure 1c; Figure S3e, Supporting Information). The general trend of decreasing ionic conductivity with voltage (Figure S3f, Supporting Information) is also consistent with the inverse of resistance trend (Figure 1c). However, it is worth noting that although the pressurized cell inhibits the global decomposition current (Figure 1a), a slight decrease of ionic conductivity from 5 mS cm^{-1} at 3 V to 4 mS cm^{-1} at 5 V, and a slightly faster decrease to 2 mS cm^{-1} from 5 to 10 V are still observed, suggesting small local decompositions without a global charge transfer, especially in the high voltage range. Interestingly, comparing these results with

the previous performance of core-shell constrained LGPS, it appears that cell-level constrictions can provide an even greater level of mechanical stabilization than what was achievable with the material-level constriction. As discussed below, this is believed to be due to the addition of cell-level factors that provide a kinetic stability, also related to the small local decomposition implied from the electrochemical analyses, above the circa 4 V limit for mechanically induced metastability.

The synchrotron XRD of LGPS from the pressurized cell and liquid cell, as shown in Figure 1d, indicates the general crystal structure of LGPS after CV test up to 9.8 V in the pressurized

cell remains unchanged. All batteries were scanned back to 2.5 V before synchrotron XRD (SXR) measurements; therefore, the lithium composition remains the same in LGPS. Thus, as expected, no obvious peak shift is observed from SXR, and the lattice parameters from refinements have negligible changes as shown in Table S1, Supporting Information. In comparison, the liquid electrolyte Swagelok cell shows a complete decomposition of LGPS phase scanned up to 3.2 V. The purpose to use the liquid electrolyte Swagelok cell as the control sample is that it represents an extremely low mechanical constriction testing condition for each particle compared with the solid pellet test either in a Swagelok or pressurized cell, as ceramic LGPS particles can expand freely in decomposition into the liquid region. Decompositions can, thus, propagate the entire particle, giving a complete decomposition of LGPS as unveiled by the full extinguishment of the XRD peak intensities (Figure 1d) cycled beyond the intrinsic voltage stability window of LGPS at ≈ 2.1 V.^[21]

More importantly, broadening of the XRD peaks is observed after high-voltage CV scan at 7.5 and 10 V (Figure 1e; Figure S4, Supporting Information) for pressurized cells. The peak broadening with increasing 2θ angles (Figure 1f) was found to follow the trend of strain broadening rather than size broadening. That is, the growth of the full-width-at-half-max (FWHM) as $\tan(\theta)$ suggests that unit cells were displaced away from normal positions. This effect is distinct from lattice vector compression that would uniformly compress all unit cells. Such lattice vector compression results in peak shifting caused by the externally applied uniaxial pressure and/or uniform (de)lithiation. Thus, the presence of strain broadening suggests that in addition to the expected peak shifting, due to (de)lithiation and uniaxial compression at certain experimental conditions,^[12,14,24] there also exists sources of localized strains that distort particular unit cells away from normal position. The experimental step of discharging the high voltage scanned LGPS back to 2.5 V before taking SXR was designed to maintain a constant Li composition in LGPS, so the effect of Li composition induced lattice parameter change and Bragg peak shift can be minimized, while the irreversible strain effect induced at high voltage can be most clearly observed. A schematic illustration of these key differences is depicted in Schematic S1, Supporting Information. In contrast, no obvious strain broadening was observed at 3.2 V. This provides the first direct evidence of the formation of inclusions or small local decompositions beyond the voltage stability window at high voltages, as was predicted by Fitzhugh et al.^[21] At 9.8 V, a broad background is observed while the main XRD peaks remain (Figure 1d). The broad background is partially contributed by the diffuse scattering that is likely from a more severe local structure change in LGPS at the extreme voltage.

This strain effect is further reflected in the XAS measurement and analysis. Figure 1g shows the P and S XAS peaks of pristine LGPS compared with the ones after CV scans up to 3.2 and 9.8 V in liquid or solid-state batteries. Under the conditions of no mechanical constriction in the liquid battery (denoted as 3.2V-L), both P and S show obvious peak shift toward the high energy, accompanied with obvious peak shape change, indicating a significant global oxidation reaction and a rearrangement of local atomic environment in LGPS. Whereas

the P and S peaks do not show obvious sign of oxidation in solid-state batteries, as no peak shift is observed. However, it is noticeable that the “dip” intensity increases at 2470 and 2149 eV in S and P spectra, respectively. An ab initio multiple scattering simulation of the P XAS peak from LGPS with various strain applied to the unit cell is shown in Figure 1h. A comparison between experiment and simulation suggests that the increase of the dip intensity in XAS here can be caused by the negative strain, i.e., the local compression experienced by a portion of crystalline LGPS after CV scan and hold at high voltages.

Connecting the strain broadening in XRD, the dip intensity increase in XAS, and the absence of obvious global decomposition current in the CV test up to 10 V, it suggests a physical picture about the small local decomposition within the LGPS. The application of a uniaxial stress (p_a) appears to create a mechanically constrained environment in the pellet with zero porosity (the 467 MPa@250 MPa solid cell), similar to the core-shell mechanism on the particle level discussed in previous studies,^[8,21–23] which in turn expands the stability window. Above 4 V, the XRD strain broadening and XAS intensity dips suggest that the LGPS is decaying in small inclusions, which exist either inside the bulk of each particle or on the interface between particles of a close contact under p_a . However, the limited size of these inclusions, as indicated by the absence of global transfer of Li^+ ion and electron measured by CV, suggests kinetic stability up to 10 V.

LGPS tends to expand upon decomposition.^[8,21–23] The relative volume change accompanying decomposition is referred to as the reaction strain or the reaction dilation (ϵ_{RXN}). Unlike mechanical strain, reaction strain is stress-free. That is, it results from decomposition rather than the application of a stress. However, in a mechanically constricted environment here, such a local decomposition and expansion will cause a compressive stress in the neighboring environment. In an isometric approximation, this compressive stress in the local environment of the decomposed inclusion is given by some effective bulk modulus (K_{eff}) to be $K_{\text{eff}}\epsilon_{\text{RXN}}$. It is this localized compressive stress and corresponding decomposition that is believed to induce the strain broadening observed in XRD and the dip intensity increase observed in XAS.

Thermodynamically, given an unconstrained reaction in which LGPS decomposes with a Gibbs energy change of $\Delta G_{\text{chem}} < 0$, the reaction can be inhibited by the application of a mechanical constriction if the compressive pressure satisfies

$$\Delta G_{\text{chem}} + K_{\text{eff}} \epsilon_{\text{RXN}} V > 0 \quad (1)$$

where V is the reference state volume and ϵ_{RXN} is the stress-free reaction dilation—in other words ϵ_{RXN} is the fractional volume change of LGPS following decomposition in the absence of any applied stress. The effective bulk modulus in Equation (1) is the bulk modulus of the ceramic-sulfide (K_{material}) added in parallel with the mechanical constriction as given in Equation (2)^[8]

$$K_{\text{eff}}^{-1} = K_{\text{material}}^{-1} + K_{\text{constriction}}^{-1} \quad (2)$$

The application of a uniaxial pressure is differentiated from a core-shell mechanism in how $K_{\text{constriction}}$ is generated. In a core-shell material,^[8,21–23] $K_{\text{constriction}}$ is a function of the rigidity

and geometry of the shell. In contrast, for uniaxial compression, $K_{\text{constriction}}$ is a function of the applied pressure. Thus, the full stress tensor at a given location within the composite (\vec{r}) is given to be

$$\vec{\sigma}(\vec{r}) = \begin{pmatrix} K_{\text{eff}}(p_a)\epsilon_{\text{RXN}}(\vec{r}) & 0 & 0 \\ 0 & K_{\text{eff}}(p_a)\epsilon_{\text{RXN}}(\vec{r}) & 0 \\ 0 & 0 & p_a + K_{\text{eff}}(p_a)\epsilon_{\text{RXN}}(\vec{r}) \end{pmatrix} \quad (3)$$

This pressure dependence of K_{eff} is analogous to strain hardening, where the applied pressure induces plastic deformations that increase the composite rigidity. The value of this is particularly obvious when considering the elimination of voids from the composite. Such strain hardening also explains why those pellets that were pressed at 78, 233, and 467 MPa continue to show improved stability even after the pressure is released in a normal Swagelok cell. It is not the homogenous applied pressure p_a that is responsible for the mechanical stabilization but the inhomogeneous pressure $K_{\text{eff}}\epsilon_{\text{RXN}}$. This view is supported by the strain broadening curve in Figure 1f, which suggests each lattice vector is strained on the order of 5% (volumetric strain of $\approx 15\%$) following the form $\text{FWHM} \approx 4\epsilon \tan(\theta)$. This strain value is far beyond what is capable using $p_a \approx 100$ MPa as the only stress.

Minimization of free energy in the mechanically constrained ensemble allows for calculating the expanded voltage window

and the ground state decomposition products.^[8,21,23] Using ab initio data, **Figure 2a** shows the results of such calculations for LGPS at four levels of mechanical constriction ($K_{\text{eff}} = 0, 5, 10, 15$ GPa) in the voltage range of 0–10 V. Figure 2a1 shows the energy above the hull, or the magnitude of the decomposition energy. The energy above the hull of 0 eV per atom indicates that thermodynamically the LGPS is the ground state product, whereas an elevated value indicates that the LGPS will decay. The region in which the energy above hull is nearly zero (<30 meV per atom for thermal tolerance) is seen to widen in upper voltage limit from ≈ 2.1 to nearly 4 V. Figure 2a2 shows the ground state pressure corresponding to the free energy minimization. The pressure is given by $K_{\text{eff}}\epsilon_{\text{RXN}}$, where ϵ_{RXN} corresponds to the fractional volume transformation of LGPS to the products that minimize the free energy. The ground state pressure reaches 4 GPa in the high-voltage limit at $K_{\text{eff}} = 15$ GPa, which gives a volumetric reaction strain of 27% and an average lattice strain of 9%, corresponding well to the level of local compression along c axis on the order of 10% used in the XAS simulation of strained LGPS in Figure 1h, and the 5% strain estimated from XRD strain broadening. Figure 2a3 shows the total specific lithium capacity of the ground state products, which predicts that LGPS electrolyte will not provide more lithium capacity, or make further decomposition, beyond 5 V under any K_{eff} above 15 GPa. Note that the simulations at $K_{\text{eff}} = 0$ here correspond to the LGPS particles in the liquid cell

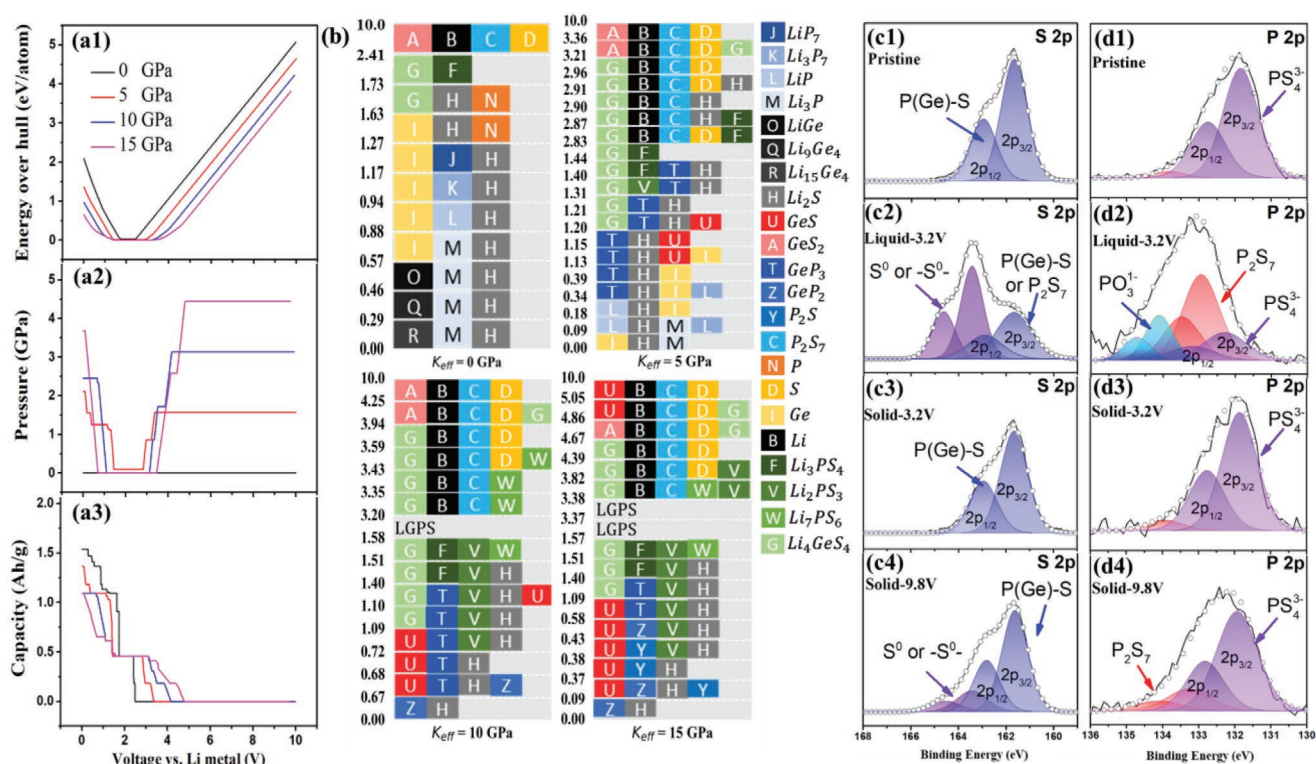


Figure 2. Decompositions of LGPS in different voltage ranges under mechanical constrictions. a1) LGPS decomposition energy, a2) ground state pressure, and a3) ground state capacity versus voltage at different effective modules (K_{eff}). b) Decomposition reaction pathways at different K_{eff} and the products induced by different phase equilibriums in different voltage ranges (see also Table S2, Supporting Information). c,d) XPS measurement of c) S and d) P element for c1,d1) pristine LGPS, c2,d2) battery after 3.2 V CV scan in liquid electrolyte, c3,d3) in pressurized solid-state cell after 3.2 V CV scan, and c4,d4) after 9.8 V CV scan. Each CV scan is followed by a 10 h hold at the corresponding cut-off voltage.

case, as well as the LGPS region near the void in the initially pressed pellets but tested in normal Swagelok cells ($p_a = 0$) in Figure 1, where decompositions of LGPS beyond the voltage window are not mechanically constricted, causing the complete decomposition of LGPS phase in the liquid cell (Figure 1d), and the small decomposition currents observed in the CV tests (Figure 1b).

The exact decomposition products predicted by DFT without considering the thermal tolerance are shown in Figure 2b in the entire voltage range at different K_{eff} , with the exact reaction equations listed in Table S2, Supporting Information. These results indicate how the decompositions resulting in inclusion formation quantitatively change under mechanical constrictions. The elemental valence states in the decompositions can thus be directly compared with the XPS measurement that are sensitive to chemical valence information on the particle surface (Figure 2c,d). This provides complementary information to the bulk sensitive XAS.

Stoichiometric LGPS is composed of nominal valence states of Li^{1+} , Ge^{4+} , P^{5+} , and S^{2-} . As LGPS undergoes the formation of lithium metal ($\text{Li}^{1+} \rightarrow \text{Li}^0$) at high voltages, remaining elements must become oxidized. For $K_{\text{eff}} = 0$ GPa, our simulation in Figure 2b suggests that sulfur in LGPS is the most likely to be oxidized, forming S^{0-} (P_2S_7) and S^0 (elemental sulfur) above 2.41 V. Note that there are two types of S bonds in polysulfides, the bridging sulfur in $\text{P}-\text{S}^0-\text{P}$ with a XPS peak at 163.5 eV and the non-bridging sulfur in $\text{P}=\text{S}$ at 162.1 eV.^[25–28] XPS peak of bridging S^{0-} (163.5 eV) or S^0 (163.9 eV)^[29] should show very similar charge state, and obviously higher than S^{2-} (161.4 eV)^[29–31] in LGPS. Therefore, the large purple peak at 163.4 eV in Figure 2c2 is likely from the oxidized sulfur in S or P_2S_7 due to the lack of mechanical constriction in the liquid battery cell. The peak at 161.6 eV in Figure 2c2 can be assigned to $\text{P}(\text{Ge})-\text{S}$ bond (161.4 eV)^[32] in LGPS, Li_3PS_4 (161.4 eV)^[33] or $\text{S}=\text{P}$ (162.1 eV)^[25] in polysulfide. Similarly, P $2p_{3/2}$ peak from LGPS is at 131.4 eV,^[34] where the P valence state is 5^+ . Although P in most $\text{Li}_x\text{Ge}_y\text{P}_z\text{S}_w$ or $\text{Li}_x\text{P}_y\text{S}_z$ compounds shows similar charge state as LGPS (Figure S5, Supporting Information), the P in $\text{P}-\text{S}$ binaries such as P_2S_7 has a higher oxidation state with the XPS peak usually at around 132.9 eV.^[33] Therefore, the red peak at around 132.9 eV in Figure 2d2 should be from P_2S_7 binaries. The light blue peak at 134.1 eV in Figure 2d2 is the oxidation of P in the liquid electrolyte, leading to the formation of $(\text{PO}_3)^{1-}$ (134.6 eV)^[33,35] rather than $(\text{PO}_4)^{2-}$ that would be at 133.3 eV. This P-O bond length is consistent with the real space analysis of XAS measurement in Figure S6, Supporting Information. The purple peak at 131.6 eV in Figure 2d2 should be assigned to the residual LGPS (131.4 eV)^[29] or the decomposed product Li_3PS_4 (131.7 eV).^[33] In the Figure 2c2,d2, the large amount of oxidized P and S XAS signals from the decomposition products of S and/or P_2S_7 is consistent with the decomposition predicted at $K_{\text{eff}} = 0$ GPa in the high voltage range in Figure 2b. This suggests that the thermodynamically favored decomposition is in fact representative of the decomposition that occurs experimentally in the liquid cell without an effective mechanical constriction.

In contrast, the calculated thermodynamic metastability limit of LGPS reaches nearly 4 V at $K_{\text{eff}} = 15$ GPa. Accordingly, there is no obvious oxidation of S and P observed in the pressurized

battery test condition of strongly constrained LGPS charged to 3.2 V and held for 10 h in Figure 2c3,d3. Recall that there is conductive carbon mixed with LGPS in the cathode region, and there is no Bragg peak broadening for SXRD of LGPS for such battery (3.2 V in Figure 1e,f). The absence of decomposition in XPS is, thus, consistent with our prediction of widened voltage metastability from 2.1 to ≈ 4 V by mechanical constriction on the order of ceramic electrolyte's mechanical modulus (20–30 GPa). In this case, LGPS is thermodynamically metastable, without obvious local decompositions that can induce local compressive strains to LGPS for an observable strain broadening. Furthermore, beyond the voltage stability limit of 4 V, the LGPS at 9.8 V shows a slight oxidation of S or P (much less than the liquid control). It is predicted that at a high K_{eff} , P_2S_7 , Li_4GeS_4 , Li_2PS_3 , and/or S are formed (e.g., Figure 2b at $K_{\text{eff}} = 15$ GPa). The XPS peak of S in Li_4GeS_4 (160.8 eV)^[36] is close to that in LGPS (161.3 eV), and the Bader charges of S (Figure S5b, Supporting Information) are close among Li_4GeS_4 , Li_2PS_3 and LGPS, they are, thus, not easy to distinguish at small decompositions. The small purple peak in Figure 2c4 at 163.2 eV should come from the elemental S or P_2S_7 . Oxidized P peak at 133.2 eV in Figure 2d4 can also be attributed to P_2S_7 . From the XPS result in the case of 9.8 V pressurized cell, one can find that the decomposition of LGPS is largely prohibited with limited small decompositions following the prediction at high K_{eff} . Given the agreement of these measurements with the 4 V thermodynamic prediction, the limited decay beyond 4 V, nonetheless, indicates that kinetic effects must be in play.

The proposed mechanism for such mechanically induced kinetic stability is depicted in Figure 3. Within a given particle of LGPS that is undergoing a local decomposition, the particle can be partitioned into three regions. The first two are the pristine and decomposed regions, while the third region is their interface (henceforth the decomposition front). The propagation direction of the decomposition front is controlled by the thermodynamic relation of Equation (1). If Equation (1) is satisfied, the front should propagate inwards, preferring the pristine LGPS and thus no decomposition/local stress. When Equation (1) is violated, the front should propagate into the LGPS and ultimately consume the particle.

However, even when Equation (1) is violated, the speed with which the front propagates into the pristine LGPS will still be influenced by the localized reaction stress. As the decomposition front propagates, there must exist ionic currents tangential to the front's curvature. This requires the presence of an overpotential to accommodate the finite conductivity of the front for each elemental species. The ohmic portion of the overpotential is given by the sum in Equation (4), where $\rho_i(p)$ is the resistivity of the front for each species i at the pressure p that is present at the front, l_i is the characteristic length scale of the decomposed morphology, and j_i is the ionic current density

$$\eta = \sum_i \rho_i(p) l_i j_i \quad (4)$$

Given that $\rho_i(p)$ can quickly grow with constriction, it is to be expected that this overpotential becomes significant at high local pressures, as illustrated in the energy landscape of Figure S7, Supporting Information. This effect can be seen by comparing the expected constriction with prior molecular dynamics results

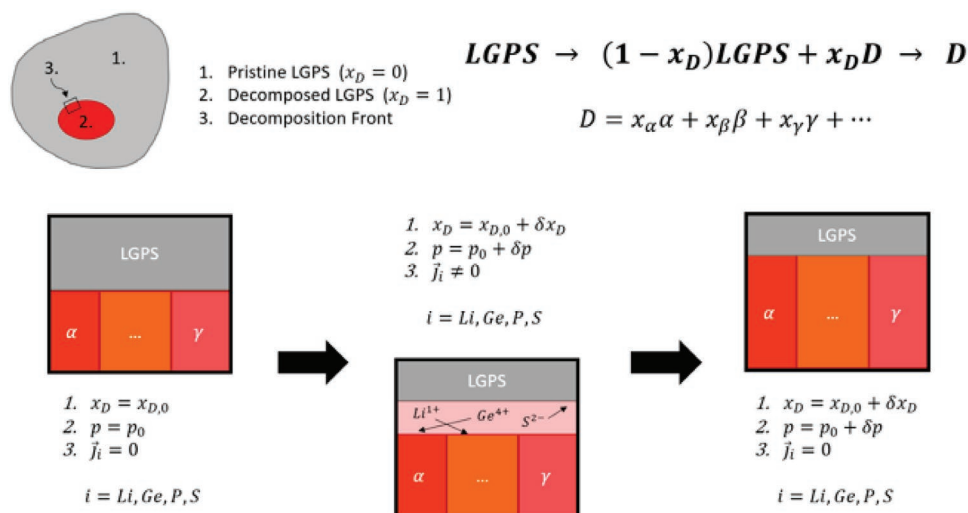


Figure 3. Illustration of restricted decomposition front propagation limited by kinetics. Pristine (gray, region 1) and decomposed (reddish, region 2) LGPS are indicated by the mole fraction of decomposed LGPS ($x_D = 1$ for purely decomposed, $x_D = 0$ for pristine). On their interface or the decomposition front (rectangular region 3 in the top-left particle, with the magnified decomposition evolution shown in the bottom three illustrations), the mole fraction transitions from 0 to 1. Decomposed phases are marked with $\alpha, \beta, \gamma, \dots$ with the corresponding fractions of $x_\alpha, x_\beta, x_\gamma, \dots$. Such propagation is seen to require tangential ionic conduction with an ionic current \vec{j}_i for each elemental species in the decomposition front (pink region in the bottom-middle illustration).

of constricted cells.^[37] The pressure on the decomposition front is given by $p = K_{\text{eff}} \epsilon_{\text{RXN}}$ and the elastic volume strain of the material at that compressive pressure is $p = K_{\text{material}} \epsilon_V$. Since the strain of a single lattice vector is approximately $\epsilon = \frac{1}{3} \epsilon_V$, the strain of LGPS near the front is expected to be on the order of $\epsilon \approx \frac{K_{\text{eff}}}{K_{\text{material}}} \frac{\epsilon_{\text{RXN}}}{3}$. For well constrained systems where $K_{\text{eff}} \approx K_{\text{material}}$, this strain can easily reach the 4% simulated by Ong et al.,^[37] as ϵ_{RXN} can easily exceed 30% at high voltages for LGPS. Given that the activation energy for Li migration in LGPS is predicted to increase from 230 meV to 590 meV^[37] upon constriction by 4%, the rate at which lithium reordering can occur decreases by a factor of $\exp\left(-\frac{590 \text{ meV}}{k_B T}\right) / \exp\left(-\frac{230}{k_B T}\right) \approx 10^{-6}$ at room temperature. This many orders of magnitude reduction in the ionic interdiffusion rate can explain why, for any voltage up to 10 V, the pressurized cell showed virtually no global decomposition current.

Encouraged by these critical understandings, the following high-voltage solid-state battery cells were developed. **Figure 4** shows the galvanostatic cycling along with their cyclability performance of all-solid-state batteries, using LCO, LNMO, and LCMO as cathodes; LGPS as the electrolyte and separator; and LTO as the anode. The battery tests were performed in the pressurized cell, where the cells were initially pressed with 467 MPa and then fastened in bolted pressurized cells at round 250 MPa for battery tests. LCO is the most commonly and widely used cathode material for commercial Li-ion batteries, with a plateau at ≈ 4 V against Li^+/Li , whereas LNMO is considered as one of the most promising high voltage cathode materials with a flat operating voltage at 4.7 V versus Li^+/Li . The charge and discharge curves of LCO and LNMO are depicted in Figure 4a1,a2, respectively. Both batteries show a flat working plateau centered at 2 V (3.5 V vs Li^+/Li) for LCO, and at 2.9 V (4.4 V vs Li^+/Li)

for LNMO in the first discharge. Moreover, both of them exhibit good cyclabilities in Figure 4b1,b2, with a capacity fading of 9% in the first 360 cycles for LCO and 18% in the first 100 cycles for LNMO. This indicates that the decomposition or interfacial reaction of the cathode materials with LGPS is well controlled. Note that LiNbO_3 coating was applied to all cathode materials (Figure S8, Supporting Information). The all-battery systems also show a good rate capability up to 1 C, corresponding to 0.38 mA cm^{-2} (Figure S9, Supporting Information). These results are in agreement with the CV tests reported in Figure 1, where it was shown that mechanical constriction can inhibit the decomposition of LGPS and widen its operational voltage range to much higher values than those previously reported.^[8]

We want to emphasize that there are actually various strains in this solid-state battery system, including volume and thus porosity change in the LGPS part of the ceramic pellet in response to external and internal pressures, decomposition reaction strain of LGPS at high or low voltages, lattice parameter and thus volume change of cathode materials at different lithium compositions, and reaction strain from the cathode-electrolyte interface. Those strains collectively influence the electrochemical stability of the battery system. Based on our understanding, a positive local strain generally may lead to a metastable state to inhibit the further propagation of detrimental reactions, while a negative strain has to be compensated by a positive strain locally. For example, the compressed LGPS in the battery pellet by the pressurized cell should compensate the local volume shrinkage of LNMO^[38,39] during the battery charge by the local expansion of LGPS. If such compensation is not sufficient locally, however, thermodynamically preferred interface reactions or LGPS decomposition will occupy the gap volume, leading to higher interface resistance and worse cycling performance. Note that a +2.6% *c*-axis expansion between the charged and discharged states is observed from

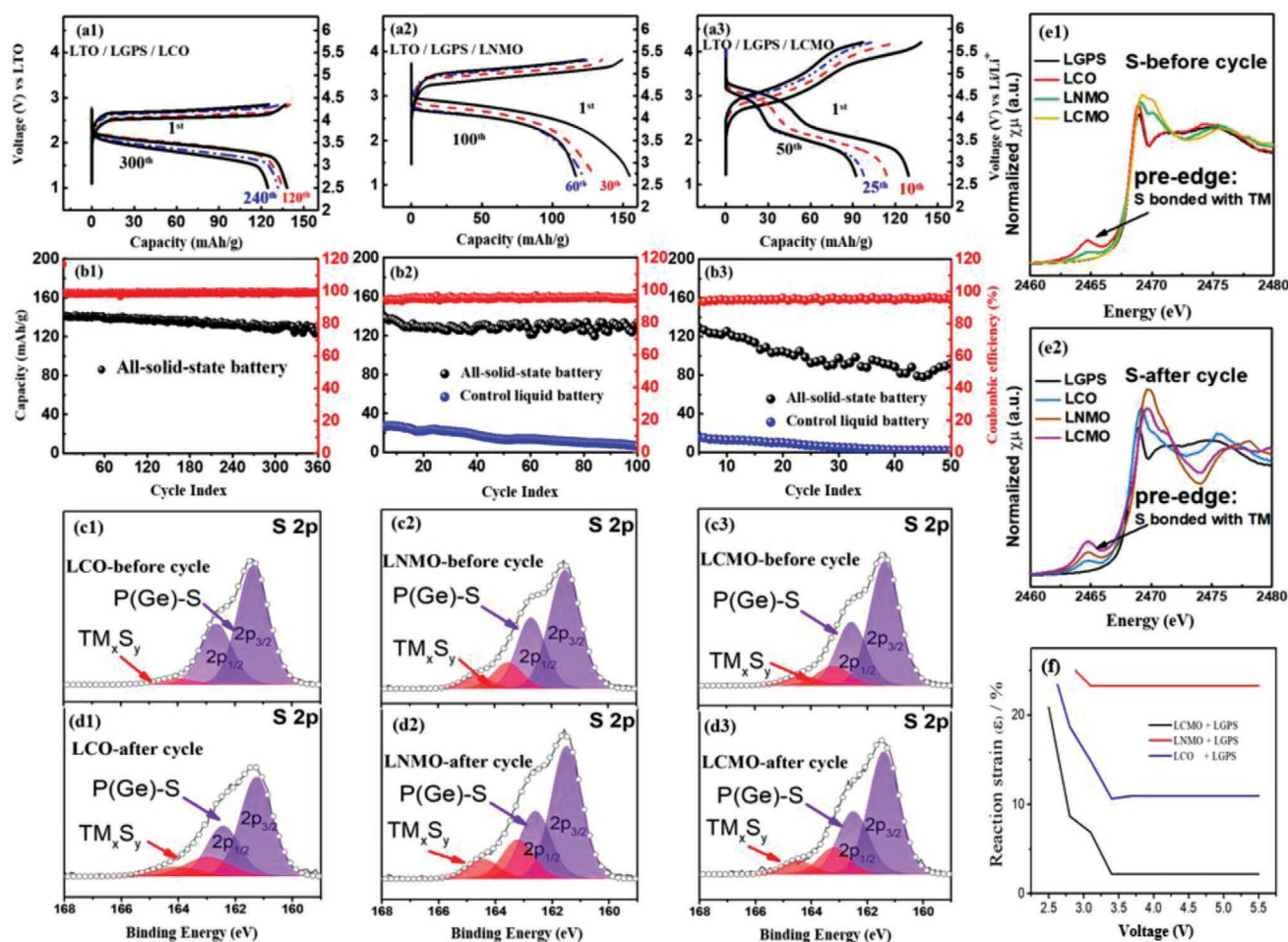


Figure 4. Electrochemical performance and characterization of the solid-state batteries. a) Galvanostatic charge and discharge voltage curves for all-solid-state batteries using a1) LCO, a2) LNMO, and a3) LCMO as cathode materials versus LTO. b) The cyclability of the batteries is represented in (b1), (b2), and (b3) for LCO, LNMO, and LCMO, respectively. Here, LCO and LNMO are charged and discharged at 0.3 C, whereas LCMO is charged at 0.3 C and discharged at 0.1 C. All batteries are tested at room temperature, in the pressurize cell initially pressed with 467 MPa and tested at 250 MPa. Active materials are coated with LiNbO_3 (LNO), as shown in Figure S8, Supporting Information. c, d) XPS measurements of LCO, LNMO, and LCMO-LGPS before and after five cycles. e) XAS measurements of LCO, LNMO, and LCMO-LGPS e1) before and e2) after five cycles for the element of S. f) Simulated interface reaction strains of LCO-LGPS, LCMO-LGPS, and LNMO-LGPS in the voltage range of 2.5–5.5 V at $K_{\text{eff}} = 0$ GPa. The strains are calculated based on the volume of decomposition products in Table S3, Supporting Information.

the hexagonal-monoclinic phase change of LCO,^[40] while a -0.92% ^[38] and a -0.8% ^[39] shrinkage are associated with LNMO and LCMO spinel cathodes, respectively, at the charged state. Although the volume shrinkage of charged LNMO/LCMO particle can be partially compensated by the local expansion of surrounding LGPS under mechanical constriction, as a reverse process of Figure S1, Supporting Information, any imperfect compensation will still lead to a local stress release and thus a propagation of the interface reaction, causing the degraded cycling performance than LCO, besides the contribution from voltage differences between these cathodes.

Moreover, to further probe the stability of LGPS and the complexity on the interfaces, LCMO cathode was synthesized as it presents a working plateau above 5 V in charge. Figure 4a3 depicts the battery test curves of LCMO versus LTO. In both charge and discharge profiles, two plateaus can be observed centered at ≈ 2.2 and ≈ 3.2 V (3.7 and 4.7 V vs Li^+/Li) in the discharge curve of the first cycle, which are associated with the

oxidation reactions of $\text{Mn}^{3+}/\text{Mn}^{4+}$ and $\text{Co}^{3+}/\text{Co}^{4+}$, respectively.^[41] The structures of both LCMO and LGPS are stable after 50 cycles from XRD measurements (Figure S10, Supporting Information). As shown in Figure 4b3, however, upon cycling a capacity fading around 33% in 50 cycles is observed, which has to be attributed to the interface reaction between LCMO and LGPS at high voltages, due to possibly imperfect LiNbO_3 (LNO) coating and other equally important strain-related factors that will be discussed later. However, what we want to first emphasize here is that in contrast to previous reports claiming a narrow stability window of LGPS, we show that LGPS can be used as the electrolyte material in high-voltage-cathode all-solid-state batteries upon a mechanical constriction, showing cyclable performance even when the charging plateau is as high as 5.3 V versus Li^+/Li .

We now focus on the more challenging interface chemical and electrochemical stability issues between cathodes and LGPS. Note that the chemical reaction between LGPS and the

cathode material happens as soon as the materials come in contact during the cathode film assembly. This is in contrast with the electrochemical reactions that do not occur until the external circuit assembly is attached. Thus, a major difference between the two is that chemical reactions occur before pressurization/cell assembly, whereas the electrochemical reactions occur afterwards. Figure 4c1–d3 show the XPS measurements of S in LGPS before and after battery cycles using LCO, LNMO, and LCMO as cathodes, respectively. Each element can become oxidized either by the chemical reaction with the cathode material (chemical oxidation) or the delithiation of the LGPS by the application of a voltage (electrochemical oxidation). The presence of oxidized sulfur in the pristine samples is indicative of the degree of chemical reaction with the cathode material. The XPS peak of transition metal (TM) bonded S is around 162.9 eV; therefore, the red peaks in Figure 4c1–d3 are attributed to S in TM–S compound (163 eV) formed after the interface (electro)chemical reaction. Note that after electrochemical cycling, the signal of TM–S bond becomes stronger, indicating that the sulfur was further electrochemically oxidized. XAS measurement shows a pre-edge for the S element (Figure 4e), while no such pre-edge was observed for P, suggesting that S, instead of P, is bonded with transition metal from either coating or cathode materials. For the LCO–LGPS battery, both XPS and XAS measurements indicate that the decomposition is not severe in either surface or bulk, giving the best cycling performance. This is partly contributed by both the low working voltage and the unique positive delithiation strain of LCO among the three types of cathodes.

It is important to note, however, that the intensity of XAS S pre-edge is increased more significantly for LCMO than LNMO after cycling, while in XPS the TM–S peak shows the opposite trend. Table S3, Supporting Information, lists the decomposition products of the interface reactions at no mechanical constriction ($K_{\text{eff}} = 0$) between cathode materials and LGPS at different voltages, from which an interface reaction strain can be evaluated (Figure 4f). The simulation results show that LNMO–LGPS interface has a positive reaction strain at around 25% while LCMO–LGPS is only at 2%. LCO shows an intermediate reaction strain around 10%. The interface reaction can then be limited between either LCO or LNMO and LGPS due to the large positive interface reaction strain under a proper mechanical constriction condition, while it might not be effectively inhibited for the LCMO–LGPS interface. Considering that LCMO shows the worst cycling performance among the three cathode materials, and as mentioned earlier, that the penetration depth of XAS is much higher than the surface sensitive XPS, our results indicate that the interface electrochemical decomposition reaction propagates deeper into the LGPS and LCMO particles, i.e., a thicker interface decomposition layer, which is detrimental to the cycling performance. While in the case of LNMO–LGPS battery, the decomposition is limited more on the interface with a more concentrated positive reaction strain to prevent LGPS from further decomposition.^[23,42] Therefore, it is the propagating behavior of an interface decomposition that is more relevant to the decay of battery performance comparing LNMO and LCMO, while LCO shows the most stable interface due to both the positive delithiation strain of LCO and the positive interface reaction strain with LGPS, besides the lower cathode voltage than LNMO and LCMO.

We further simulate both chemical and electrochemical stabilities of interfaces using the pseudo-phase method.^[11,42–44] Figure S11a and Table S4, Supporting Information, give the results for chemical reaction pseudo-phase calculations for LGPS+LNO, LCO, LNMO, and LCMO, which represent the decomposed interface, or interphase, with the chemical reaction energies of 124, 345, 322, and 335 meV per atom, respectively. Despite being coated with LNO of a much lower reaction energy, LNO and LGPS interface is still thermodynamically reactive when without a proper mechanical constriction. In addition, the coating might not be perfect, allowing some contact with LGPS. Thus, either a low level of local mechanical constriction (i.e., around a void in the LGPS–cathode pellet) or imperfect coating can result in the chemical oxidation of sulfur seen in the pristine samples of Figure 4c–e. The predicted decomposition products (Table S4, Supporting Information) also support the preferred binding between transition metal elements and sulfur (TM_xS_y), as observed in both XPS and XAS measurements (Figure 4).

The interphase can be used to calculate how the decomposed interface will further decay as the battery is cycled at various mechanical constriction levels. For example, Figure S11b,c, Supporting Information, shows the electrochemical stability of the LGPS and LNO interphase at various K_{eff} . Similar results can be found for LGPS and cathode interphases. It is found that such interphase also experiences mechanically induced metastability, with LCMO showing weaker metastability than LNMO and LCO, consistent with the reaction strain analysis in Figure 4f.

Thus, in a full cell, the proper constriction should lead to mechanically induced metastability both within the bulk of the solid-electrolyte (Figures 1 and 2), and at the interface with the cathode materials (such as the LCO and LNMO batteries in Figure 4). The importance of the LNO coating, however, is that first, it reduces the interface reaction energy with LGPS at $K_{\text{eff}} = 0$ (Figure S11a, Supporting Information), and shows a further mechanically induced metastability in a widened voltage window at $K_{\text{eff}} > 0$ (Figure S11b, Supporting Information); second, LGPS interfaces are more likely to experience mechanically induced metastability with insulators (such as LNO) than with conductors (such as LCO, LNMO, and LCMO). One reason for this is that when the interphase oxidizes to form lithium metal, the lithium metal (or in an alloy form with other elements) is likely to form locally if the interface is between two electronically insulating materials, rather than migrating to the anode in the electronically conducting case.^[21] This contributes to a larger local volume change and, hence, a larger reaction dilation for a more effective mechanically induced metastability on the interface.

We further pair these cathodes with lithium metal anode using the graphite protection technique recently developed for the mechanical constriction design on the anode side.^[22] Lithium metal–LCO batteries were compared at different mechanical conditions using Teflon Swagelok, aluminum (Al) pressurized cell and stainless-steel (SS) pressurized cells at an external pressure of around 3–5, 20, and 100–200 MPa, respectively, as shown in Figure S12, Supporting Information. The external pressures applied by the three devices range from several MPa to several hundred MPa, with the SS cell showing the

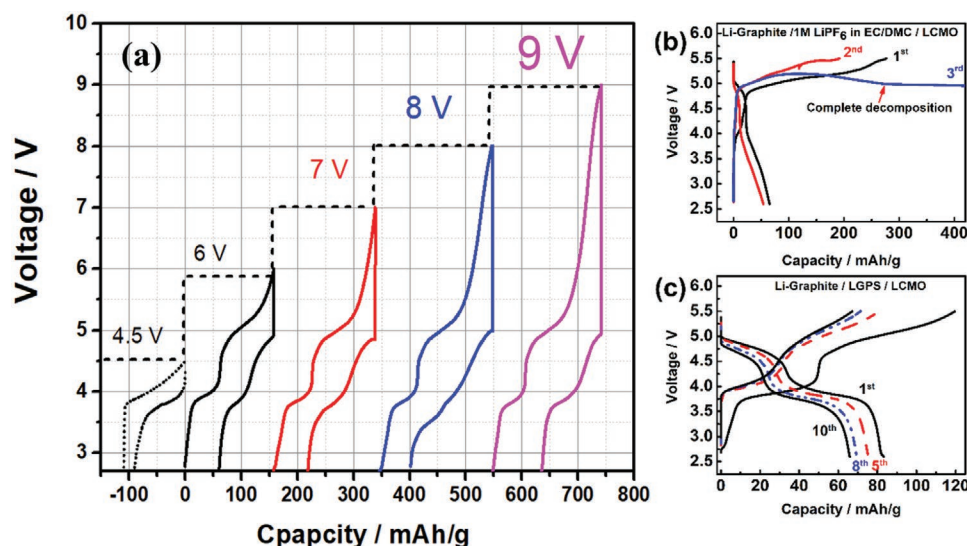


Figure 5. High-voltage performance of the solid-state batteries compared with liquid electrolyte batteries. a) Galvanostatic charge and discharge profiles for all-solid-state batteries using LCO and LCMO as cathode and graphite-coated lithium metal as anode, with cut-off voltage from 2.6–4.5 V (LCO) and 2.6–(6–9) V (LCMO). The batteries are charged at 0.3 C and discharged at 0.1 C. Cycling performance of LCMO lithium metal battery using b) 1 M LiPF₆ in EC/DMC and c) constrained LGPS as electrolyte, with cut-off voltage from 2.5–5.5 V at a charge rate of 0.3 C and a discharge rate of 0.1 C.

strongest capability for constriction and the highest capacity. Obvious fluctuation in voltage profile and a long decomposition plateau is observed in the battery tested in Swagelok, while the decomposition plateau is shortened for the Al-pressurized cell and excluded for the SS cell. This is a direct evidence from battery system level that mechanical constriction can stabilize bulk and interface electrochemical decompositions. A similar structure was applied to make the higher-voltage lithium metal battery using LCMO as cathode in the SS-pressurized cell, where the cell was initially pressed with 467 MPa and fastened at 250 MPa for further battery test. It is shown in Figure S13, Supporting Information, that graphite protection layer alleviate the interface reaction between lithium metal and LGPS.^[34]

Figure 5a shows the battery performance of LCO and LCMO-LGPS-(graphite)Li batteries. The LCMO cathode can be charged and polarized up to 9 V, which simulates the high-voltage charge status of not-yet-discovered high-voltage redox chemistries. Discharging capacities of 99, 120, 146, and 111 mAh g⁻¹ are obtained by charging LCMO to 6, 7, 8, and 9 V, respectively, (Figure 5a). Although there are more side reactions after the battery is charged to voltages above 8 V, the battery is seen to maintain the discharge capability even up to 9 V. This high-voltage charge and discharge of LCMO-LGPS battery demonstrates the high electrochemical window of over 9 V for constrained LGPS solid-state battery system. At highly delithiated state, cathode materials usually show poor electrochemical stability and the reaction between cathode material and electrolyte is also more severe;^[45] therefore, at such high voltage, a more specialized interface coating has to be designed.^[42,46,47] Nevertheless, it shows the opportunity to design the battery at a voltage far beyond the electrochemical window of liquid electrolyte. To contrast this performance with conventional electrolytes, Figure 5b depicts organic liquid electrolyte failing at nearly 5 V. A solid battery cycling at 5.5 V and tested in the

pressurized cell with 250 MPa external pressure (Figure 5c), however, shows a cyclable result and high Coulombic efficiency even at high cut-off voltage of 5.5 V, in contrast to the liquid battery. Although the performance of Li(graphite)-LCMO battery is not as good as the full battery due to the mechanical softness of lithium metal, this result still shows that, unlike liquid electrolytes, solid-state electrolytes are a better platform to run high-voltage cathode materials under a proper design of mechanical constrictions.

In summary, we have demonstrated how mechanical constriction can widen the stability of ceramic solid electrolytes. This results in a controllable increase of the electrochemical window to levels far beyond organic liquid electrolytes. CV tests show that properly designed solid-state electrolytes working under quasi-isovolumetric conditions can operate up to nearly 10 V versus lithium metal. A mechanism for this mechanically induced kinetic stability effect in sulfide solid-electrolytes is proposed based on a careful comparison between experimental characterizations and DFT simulations. It is revealed that the solid-state system can be kinetically stabilized under a mechanically constrictive environment. Moreover, based on this understanding, it has been shown how several high-voltage solid-state battery systems, using some of the most commonly used and/or promising cathode materials, can operate up to 9 V following the mechanical constriction design principle. Therefore, the development of high-voltage solid-state batteries is not compromised by the stability of the electrolyte material, but rather is relied on a proper design of mechanical constrictions on the battery system level that collectively considers electrode and electrolyte materials, the multiple interfaces, as well as the battery cells. We anticipate that this work as a catalyst for the development of new energy storage systems and new cathode materials focused on ultra-high voltage electrochemistry.

3. Experimental Section

XRD and SXRD Characterization: XRD data were collected in a Rigaku MiniFlex 6G diffractometer working at 45 kV and 40 mA, using Cu K α radiation (wavelength of 1.54056 Å). The working conditions were 2 θ scanning between 10° and 80°, with a 0.02° step and a scan speed of 0.24 s per step.

Synchrotron high-energy XRD measurements were performed at the 11-ID-C beamline of the Advanced Photon Source at Argonne National Laboratory to investigate the crystal structural change as a function of cycling voltages or external pressures. High-energy X-rays with a 0.1173 Å wavelength were utilized to obtain 2D diffraction patterns in the transmission geometry using a PerkinElmer large area detector (2048 pixels \times 2048 pixels) placed downstream at 1.5 m away from the sample. The scattering parameters including the sample to detector distance and detector geometry collection were calibrated using a standard CeO₂ powder. The data processing by converting 2D diffraction patterns into 1D data curve was obtained by FIT2D data reduction software.

SEM and XPS Characterization: Cross-sectional imaging of LGPS pellet was obtained by a Supra 55 SEM. The samples were mounted onto a standard SEM stub and sealed into plastic bags inside an argon-filled glove box. The XPS samples after CV test or battery cycling were scratched from the pellet first and then mounted onto a standard XPS sample holder. The XPS was obtained from a Thermo Scientific K-Alpha⁺ spectrometer. All XPS results are fitted by peak-differentiating and imitating via Avantage, where the PS₄³⁻ peaks in Figure 2c3–d4 were aligned using C 1s peak and pristine LGPS peak.

XAS Characterization: Ex situ measurements of P K- and S K-edges were performed at the Advanced Photon Source on the bending-magnet beamline 9-BM-B with electron energy of 7 GeV and average current of 100 mA. The radiation was monochromatized by a Si (111) double-crystal monochromator. At the S K-edge, spectra were collected in fluorescence mode using a four-element vortex detector. All samples were measured in helium-filled chamber. The X-ray absorption near-edge structure (XANES) and extended X-ray absorption fine structure (EXAFS) spectra were processed using the Athena software package.^[48] XAS simulation was performed using FEFF9 software package.

Electrochemical Characterization: LGPS in this work was purchased from MSE Supplies LLC without a post-processing step for the core-shell structure. Conductive carbon black used in this work was Super C65 from Imerys; no treatment was conducted prior to assembly. For the LGPS+C/LGPS part, the pellets were made by pressing 100 mg LGPS powder at 78, 233, and 467 MPa, respectively, a lithium metal coated with Li₃PS₄ or with graphite was attached to the pellet and tightened into Swagelok or the homemade pressurized cell. The coating process is described in our previous work.^[8] The pressure applied by a Swagelok battery was 3–5 MPa, while the pressurized cell can apply up to 250 MPa during battery tests. A total of 4 mg C/LGPS composite cathode (weight ratio = 1:9) was used as the cathode, while Li/graphite (weight ratio = 1:4)^[22] was applied as an anode for the pressurized cell to prevent lithium penetration. The weight of electrolyte and composite cathode was constant for all the pellets. In the CV test, voltage starting from the open circuit voltage to 9.8 V was ramped at the scan rate of 0.1 mV s⁻¹, during which the decomposition current at each voltage was measured. The decomposition current was normalized to the LGPS in the cathode part. The CV test was conducted on a Solartron 1470E electrochemical test system between OCV to 3.2, 7.5, and 9.8 V, respectively. Each CV scan was followed by a voltage hold for 10 h to fully develop the decomposition, and then it was scanned back to 2.5 V before any further characterizations. The electrochemical impedance spectroscopy (EIS) was conducted on Solartron 1260A impedance analyzer in the frequency range of 3 MHz to 0.1 Hz.

For all-solid-state batteries, the electrode and electrolyte layers were made by the dry method, which employs polytetrafluoroethylene (PTFE) as the binder and allows to obtain films with a typical thickness of 100–200 μ m. Additionally, two different kinds of all-solid-state batteries were assembled, using Li₄Ti₅O₁₂ (LTO) or lithium (Li) metal as anode. In either case, the composite cathode was prepared by mixing the active

materials (LiCo_{0.5}Mn_{1.5}O₄, LiNi_{0.5}Mn_{1.5}O₄, or LiCoO₂) and Li₁₀GeP₂S₁₂ (LGPS) powder in a weight ratio of 70:30 with an extra 3% of PTFE. This mixture was then rolled into a thin film. For those all-solid-state batteries using LTO as anode, a separator film of LGPS mixed with PTFE was employed with a weight ratio of 95:5. The anode composition consists of a mixture of LGPS, LTO, and carbon black at a weight ratio of 60:30:10 and an extra 3% of PTFE. The Swagelok battery cell of cathode film (using LiCo_{0.5}Mn_{1.5}O₄, LiNi_{0.5}Mn_{1.5}O₄, or LiCoO₂ as active material)/LGPS film/LTO film was then assembled in an argon-filled glove box. The specific capacity was calculated based on the amount of LTO (30 wt%) in the anode film. The galvanostatic battery cycling test was performed on an ArbinBT2000 workstation at room temperature. When lithium metal was used as anode, a Li metal foil with a diameter and thickness of 5/16" and 40 μ m, respectively, was applied onto the current collector. In order to prevent interface side reactions, the Li foil was covered by a 3/8" diameter graphite film with a weight ratio of graphite and PTFE as 96:4. After loading the negative electrode into a Swagelok battery cell, 70 mg of pure LGPS powder was added and slightly pressed, which acts as a separator. Finally, \approx 1 mg film of the cathode composite LCMO was added and pressed up to 467 MPa to form the battery, whose final configuration was LCMO/LGPS pellet/graphite film+Li metal. For high-voltage test in Figure 5a, the battery was charged at 0.3 C followed by a 30 min rest and then discharged at 0.1 C. All batteries in this study were tested at room temperature, except for batteries in Figure 5, which were tested at 55 °C.

Liquid control batteries were assembled using glass fiber as separator and 1 M LiPF₆ in EC/DMC (v:v = 1:1) as electrolyte. For the CV test, a 4 mg film with LGPS:C:PTFE = 88:9:3 was applied as cathode. For the liquid battery testing, a 2 mg cathode film with active materials (LCMO or LNMO):PTFE = 95:5 was applied. The powder of cathode materials was first mixed with PTFE, and then rolled into a thin film with diameter of 5/16". The same Li/graphite as described before or a LTO film with weight ratio of LTO:C:PTFE = 85:10:5 was applied as anode. The LTO film follows the same method as making the cathode film. The LCMO (LNMO)-separator/electrolyte-Li (LTO) battery was assembled in a Swagelok cell. The batteries were cycled at room temperature.

Computational Simulation: All ab initio calculations of phase data were obtained following the Material Project calculation guidelines in the Vienna Ab initio Software Package (VASP).^[49,50] The mechanically induced metastability calculations were performed on the computational platform we developed following the Lagrangian optimization methods outlined by Fitzhugh et al.^[21,23] Pseudo-phase calculations were performed following the methods mentioned in other studies.^[11,43,44]

Supporting Information

Supporting Information is available from the Wiley Online Library or from the author.

Acknowledgements

The work was supported by Dean's Competitive Fund for Promising Scholarship at Harvard University and the Global Innovation Contest (GIC) of LG Chem, Ltd. L.Y. thanks Baohong Chen for measuring the density of pellets. The SEM and XPS experiments were conducted at the Center for Nanoscale Systems (CNS) at Harvard University, supported by the National Science Foundation. Y.S. acknowledges the support from Chinese Scholarship Council (CSC) and the home institution of Tsinghua University as a visiting graduate student at Harvard University for 1 year. T.Q. acknowledges the support of Peking University as a visiting undergraduate student at Harvard University. H.S. acknowledges the support of Nankai University as a visiting undergraduate student at Harvard University. E.G.-G. thanks Real Colegio Complutense (RCC) at Harvard for her postdoctoral fellowship. This research used resources of the Advanced Photon Source, a U.S. Department of Energy

(DOE) Office of Science User Facility operated for the DOE Office of Science by Argonne National Laboratory under contract no. DE-AC02-06CH11357. E.H. was supported by the Assistant Secretary for Energy Efficiency and Renewable Energy, Vehicle Technology Office of the U.S. Department of Energy through the Advanced Battery Materials Research (BMR) Program, including Battery500 Consortium under contract DE-SC0012704. This research used beamline 9BM of the Advanced Photon Source, a U.S. Department of Energy (DOE) Office of Science User Facility operated for the DOE Office of Science by Argonne National Laboratory under contract no. DE-AC02-06CH11357.

Conflict of Interest

The authors declare no conflict of interest.

Author Contributions

L.Y. and W.F. contributed equally to this work. X.L. conceived the project and supervised all aspects of the research. L.Y. designed the experimental platform for the pressurized cell test. W.F. designed the computational platform for the reaction prediction modulated by mechanical constriction. L.Y., E.G.-G., Y.S., and H.S. performed electrochemical battery tests. L.Y., E.G.-G., and Y.W. conducted sample preparation and XPS and SEM characterization. W.F. and Y.W. performed the DFT simulation. T.Q. performed the XAS simulation. H.Z. conducted the SXRD characterization. L.M. and E.H. performed the XAS characterization. All authors discussed the results. L.Y., W.F., and X.L. analyzed the results and wrote the manuscript.

Keywords

high voltages, kinetic stabilities, metastability, solid-state batteries

Received: May 8, 2020

Revised: July 3, 2020

Published online:

- [1] G. Hautier, A. Jain, S. P. Ong, B. Kang, C. Moore, R. Doe, G. Ceder, *Chem. Mater.* **2011**, *23*, 3495.
- [2] A. Kraysberg, Y. Ein-Eli, A. Kraysberg, Y. Ein-Eli, *Adv. Energy Mater.* **2012**, *2*, 922.
- [3] J. B. Goodenough, K. S. Park, *J. Am. Chem. Soc.* **2013**, *135*, 1167.
- [4] Z. Wu, L. Jiang, W. Tian, Y. Wang, Y. Jiang, Q. Gu, L. Hu, *Adv. Energy Mater.* **2019**, *9*, 1900111.
- [5] J. Janek, W. G. Zeier, *Nat. Energy* **2016**, *1*, 16141.
- [6] F. Han, Y. Zhu, X. He, Y. Mo, C. Wang, *Adv. Energy Mater.* **2016**, *6*, 1501590.
- [7] N. Kamaya, K. Homma, Y. Yamakawa, M. Hirayama, R. Kanno, M. Yonemura, T. Kamiyama, Y. Kato, S. Hama, K. Kawamoto, A. Mitsui, *Nat. Mater.* **2011**, *10*, 682.
- [8] F. Wu, W. Fitzhugh, L. Ye, J. Ning, X. Li, *Nat. Commun.* **2018**, *9*, 4037.
- [9] Y. Kato, S. Hori, T. Saito, K. Suzuki, M. Hirayama, A. Mitsui, M. Yonemura, H. Iba, R. Kanno, *Nat. Energy* **2016**, *1*, 16030.
- [10] S. Wenzel, S. J. Sedlmaier, C. Dietrich, W. G. Zeier, J. Janek, *Solid State Ionics* **2018**, *318*, 102.
- [11] Y. Zhu, X. He, Y. Mo, *J. Mater. Chem. A* **2016**, *4*, 3253.
- [12] T. K. Schwietert, V. A. Arszelowska, C. Wang, C. Yu, A. Vasileiadis, N. J. J. de Klerk, J. Hageman, T. Hupfer, I. Kerkamm, Y. Xu, E. van der Maas, E. M. Kelder, S. Ganapathy, M. Wagemaker, *Nat. Mater.* **2020**, *19*, 428.
- [13] F. Du, X. Ren, J. Yang, J. Liu, W. Zhang, *J. Phys. Chem. C* **2014**, *118*, 10590.
- [14] D. H. S. Tan, E. A. Wu, H. Nguyen, Z. Chen, M. A. T. Marple, J. M. Doux, X. Wang, H. Yang, A. Banerjee, Y. S. Meng, *ACS Energy Lett.* **2019**, *4*, 2418.
- [15] J. M. Doux, Y. Yang, D. H. S. Tan, H. Nguyen, E. A. Wu, X. Wang, A. Banerjee, Y. S. Meng, *J. Mater. Chem. A* **2020**, *8*, 5049.
- [16] J. M. Doux, H. Nguyen, D. H. S. Tan, A. Banerjee, X. Wang, E. A. Wu, C. Jo, H. Yang, Y. S. Meng, *Adv. Energy Mater.* **2020**, *10*, 1903253.
- [17] R. Koerver, W. Zhang, L. De Biasi, S. Schweidler, A. O. Kondrakov, S. Kolling, T. Brezesinski, P. Hartmann, W. G. Zeier, J. Janek, *Energy Environ. Sci.* **2018**, *11*, 2142.
- [18] R. Garcia-Mendez, J. G. Smith, J. C. Neufeind, D. J. Siegel, J. Sakamoto, *Adv. Energy Mater.* **2020**, *10*, 2000335.
- [19] J. Kasemchainan, S. Zekoll, D. Spencer Jolly, Z. Ning, G. O. Hartley, J. Marrow, P. G. Bruce, *Nat. Mater.* **2019**, *18*, 1105.
- [20] R. Garcia-Mendez, F. Mizuno, R. Zhang, T. S. Arthur, J. Sakamoto, *Electrochim. Acta* **2017**, *237*, 144.
- [21] W. Fitzhugh, F. Wu, L. Ye, H. Su, X. Li, *Small* **2019**, *15*, 1901470.
- [22] Y. Su, L. Ye, W. Fitzhugh, Y. Wang, E. Gil-González, I. Kim, X. Li, *Energy Environ. Sci.* **2020**, *13*, 908.
- [23] W. Fitzhugh, L. Ye, X. Li, *J. Mater. Chem. A* **2019**, *7*, 23604.
- [24] G. F. Dewald, S. Ohno, M. A. Kraft, R. Koerver, P. Till, N. M. Vargas-Barbosa, J. Janek, W. G. Zeier, *Chem. Mater.* **2019**, *31*, 8328.
- [25] N. Tanibata, H. Tsukasaki, M. Deguchi, S. Mori, A. Hayashi, M. Tatsumisago, *J. Mater. Chem. A* **2017**, *5*, 11224.
- [26] J. Auvergniot, A. Cassel, D. Foix, V. Viallet, V. Seznec, R. Dedryvère, *Solid State Ionics* **2017**, *300*, 78.
- [27] R. Franke, T. Chassé, P. Streubel, A. Meisel, *J. Electron Spectrosc. Relat. Phenom.* **1991**, *56*, 381.
- [28] T. Rödl, R. Wehrich, J. Wack, J. Senker, A. Pfitzner, *Angew. Chem., Int. Ed.* **2011**, *50*, 10996.
- [29] W. Zhang, F. H. Richter, S. P. Culver, T. Leichtweiss, J. G. Lozano, C. Dietrich, P. G. Bruce, W. G. Zeier, J. Janek, *ACS Appl. Mater. Interfaces* **2018**, *10*, 22226.
- [30] K. Yoon, J. J. Kim, W. M. Seong, M. H. Lee, K. Kang, *Sci. Rep.* **2018**, *8*, 80066.
- [31] F. Han, T. Gao, Y. Zhu, K. J. Gaskell, C. Wang, *Adv. Mater.* **2015**, *27*, 3473.
- [32] W. Zhang, T. Leichtweiß, S. P. Culver, R. Koerver, D. Das, D. A. Weber, W. G. Zeier, J. Janek, *ACS Appl. Mater. Interfaces* **2017**, *9*, 35888.
- [33] A. Kato, H. Kowada, M. Deguchi, C. Hotehama, A. Hayashi, M. Tatsumisago, *Solid State Ionics* **2018**, *322*, 1.
- [34] S. Wenzel, S. Randau, T. Leichtweiß, D. A. Weber, J. Sann, W. G. Zeier, J. Janek, *Chem. Mater.* **2016**, *28*, 2400.
- [35] R. K. Brow, M. R. Reidmeyer, D. E. Day, *J. Non-Cryst. Solids* **1988**, *99*, 178.
- [36] I. Seo, S. W. Martin, in *Lithium Ion Batteries—New Developments*, (Ed: I. Belharouak), IntechOpen, London **2012**.
- [37] S. P. Ong, Y. Mo, W. D. Richards, L. Miara, H. S. Lee, G. Ceder, *Energy Environ. Sci.* **2013**, *6*, 148.
- [38] W. K. Pang, N. Sharma, V. K. Peterson, J. J. Shiu, S. H. Wu, *J. Power Sources* **2014**, *246*, 464.
- [39] C. Dräger, F. Sigel, S. Indris, D. Mikhailova, L. Pfaffmann, M. Knapp, H. Ehrenberg, *J. Power Sources* **2017**, *371*, 55.
- [40] I. A. Courtney, J. R. Dahn, *J. Electrochem. Soc.* **1997**, *144*, 2045.
- [41] K. Chiba, Y. Hamada, H. Hayakawa, N. Hamao, K. Kataoka, M. Mamiya, N. Kijima, N. Ishida, Y. Idemoto, J. Akimoto, *Solid State Ionics* **2019**, *333*, 9.
- [42] W. Fitzhugh, F. Wu, L. Ye, W. Deng, P. Qi, X. Li, *Adv. Energy Mater.* **2019**, *9*, 1900807.
- [43] W. D. Richards, L. J. Miara, Y. Wang, J. C. Kim, G. Ceder, *Chem. Mater.* **2016**, *28*, 266.

- [44] Y. Wang, W. D. Richards, S. H. Bo, L. J. Miara, G. Ceder, *Chem. Mater.* **2017**, 29, 7475.
- [45] L. Ma, J. Xia, J. R. Dahn, *J. Electrochem. Soc.* **2014**, 161, A2250.
- [46] C. Chen, Y. Sun, L. He, M. Kotobuki, E. Hanc, Y. Chen, K. Zeng, L. Lu, *ACS Appl. Energy Mater.* **2020**, 3, 4708.
- [47] Z. Wu, Y. Wang, L. Zhang, L. Jiang, W. Tian, C. Cai, J. Price, Q. Gu, L. Hu, *ACS Appl. Energy Mater.* **2020**, 3, 3919.
- [48] B. Ravel, M. Newville, *J. Synchrotron Radiat.* **2005**, 12, 537.
- [49] A. Jain, G. Hautier, S. P. Ong, C. J. Moore, C. C. Fischer, K. A. Persson, G. Ceder, *Phys. Rev. B: Condens. Matter Mater. Phys.* **2011**, 84, 045115.
- [50] A. Jain, G. Hautier, C. J. Moore, S. Ping Ong, C. C. Fischer, T. Mueller, K. A. Persson, G. Ceder, *Comput. Mater. Sci.* **2011**, 50, 2295.